

Mechanistic insights into the electrochemical oxidation of acetate at noble metals

Venkata Sai Sriram Mosali¹, Hanna Soucie¹, Xiong Peng¹, Ehsan Faegh¹, Matthew Elam¹, Ian Street¹, and William E. Mustain^{1, 2, *}

¹Department of Chemical Engineering, University of South Carolina, Columbia, South Carolina 29208, USA

²Lead Contact

*Correspondence: mustainw@mailbox.sc.edu

SUMMARY

Electrochemical acetate oxidation (AcOR) offers a sustainable approach to produce renewable biofuels. While CO_2 formation is thermodynamically favored, acetate oxidation can also yield various products through the Kolbe and Hofer-Moest mechanisms, enabling the scope for modulating product formation via partial oxidation. Given the complexity of the reaction, it is crucial to understand how different reaction conditions influence the product profile. Furthermore, this process generates methyl radicals, providing insights into methane partial oxidation. The current study explores AcOR on noble metal electrodes (Pt, Pd, Au) in a 0.5 M CH_3COOK aqueous electrolyte, revealing the mechanism of product formation using potential- and time-dependent electrolysis and isotope labeling experiments. The effect of surface chemistry, ion transport, electrolyte concentration, and electrolysis techniques on product selectivity is analyzed. Additionally, the study compares product profiles from an electrolyzer cell to those obtained from model electrodes in batch cell setup.

Keywords: Electrocatalysis, acetate oxidation, Kolbe reaction, Hofer-Moest mechanism, methane activation, methyl radicals

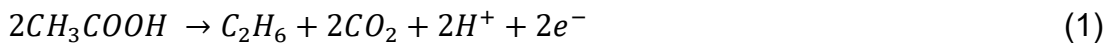
INTRODUCTION

Electrosynthesis of chemicals and fuels has gained significant research interest due to its potential to mitigate the problem of industrial CO₂ emissions and contribute to decarbonization goals when coupled with renewable energy sources.^{1,2} Biomass, as a renewable carbon source, brings an additional advantage for decarbonization when utilized for fuel generation.^{3,4} Acetate is the major biofuel generated as a byproduct during biomass upgrading.^{5,6} Over the past few decades, acetate oxidation has been extensively studied using anaerobic digestion⁷⁻⁹ as well as photocatalytic¹⁰⁻¹² and electrocatalytic methods¹³. Electrochemical partial oxidation of acetate (AcOR) can generate fuels and value-added chemicals such as ethane, ethylene, ethanol, methanol, etc. Although many experimental investigations have been conducted, the mechanistic understanding of the electrolysis of acetic acid is limited.

Faraday¹⁴, in the 1830s, was the first to observe hydrocarbon formation during the acetate oxidation reaction (AcOR). A decade later, Kolbe^{15,16} identified the primary product to be ethane and he proposed a pathway of decarboxylation followed by the coupling of two methyl groups.¹⁷ Shukla et al.^{18,19} found that the methane is also formed during electrolysis and proposed a free radical reaction mechanism for the ethane formation that was not dependent on the nature of the electrode surface. However, later studies by Fioshin et al.²⁰ and Fleischmann et al.²¹, using a rotating electrode and pulsed electrolysis experiments, respectively, over Pt electrodes proved that the electrode surface has a definitive impact on the reaction rate and product profile by controlling the adsorption/desorption of reaction intermediates. Recent theoretical investigations by the Chan group¹³ supported the argument that the reaction mechanism happens by the adsorption of reactive species on the electrode surface, followed by heterogeneous catalysis. Hence, the electrode surface, which is the active catalyst, plays a critical role in determining the reaction pathways.

AcOR begins with the breaking of the C-C bond in CH₃COOH, generating methyl radicals. Due to the complex reaction environment, the surface methyl radicals, once generated, can undergo multiple reactions and produce hydrocarbons and oxygenates via recombination, Kolbe reaction, C-C coupling and oxygenation.²² It is firmly established that the overall reaction pathway is dominated by the Kolbe reaction^{23,24}, where two

methyl radicals are combined. The overall reaction showing the decarboxylative dimerization of a pair of carboxylic acids is shown in Equation 1.



However, there are other possible reaction pathways, such as the Hofer-Moest mechanism, where non-Kolbe products are formed by the oxygenation of methyl radicals (to give alcohols) and the heterogeneous coupling of $\cdot CH_x$ ($x = 1,2,3$) radicals. Methanol, methyl acetate, formaldehyde (a resultant of over oxidation of methanol) and other products have been identified, but a detailed investigation of their formation mechanism lacks attention.²⁵ Recent studies on carboxylic acid oxidation have mostly concentrated on more complex molecules including valeric acid,^{26,27} malic acid, palmitic acid,²⁸ hexanoic acid,²⁹ and octanoate³⁰ to name a few.³¹ While preliminary studies by our group on AcOR²² revealed the formation of multiple carbon-based products, indicating a potential for complex reaction mechanisms, a comprehensive examination of the fate of methyl radicals during the oxidation reaction and the influence of catalyst surface chemistry on these mechanisms has not been undertaken.

It is also important to note that the type and concentration of the electrolyte, pH, catalyst and cell geometry can influence the AcOR reaction pathway, as has been observed in many complex electrochemical reactions such as CO₂RR, NRR, and urea synthesis.³²⁻³⁷ For instance, recent work by Nordkamp et al.³⁸ showed that the pH of the electrolyte influences the reaction pathway. Particularly under alkaline conditions, a shift of selectivity from ethane to methanol was noticed, which was attributed to the dissolution of CO₂, resulting in an enhanced concentration of bicarbonate/carbonate at the electrode/electrolyte interface. Thus, formed carbonate/bicarbonate anions inhibit Kolbe product formation. Additionally, the pH of the electrolyte influences the thermodynamic stability of the surface state of the catalyst at a given potential. For example, in the presence of water at pH 7, the Pourbaix diagram indicates that the Pt surface oxidizes to Pt(OH)₂ at 0.6 V, transitions to PtO₂ beyond 0.8 V and further oxidizes to PtO₃ above 1.2 V.³⁹ These transitions in the chemical state of the Pt surface occur at lower positive potentials in higher pH electrolytes and higher positive potentials in lower pH electrolytes. Pt(OH)₂ is stable in water and non-complexing aqueous solutions that are free from any reducing or oxidizing agents. It can oxidize hydrogen to water while converting itself to

hydrated platinic oxide. Under acidic conditions, $\text{Pt}(\text{OH})^+$ prevails while at $\text{pH} > 12$, it forms $\text{Pt}(\text{OH})_4^{2-}$.⁴⁰ On the other hand, PtO_2 can exist in various hydrated states and remains stable in non-complexing acid and neutral solutions, but under alkaline conditions, it forms $\text{PtO}_3^{2-}/\text{Pt}(\text{OH})_6^{2-}$. When anodically polarized, PtO_3 is highly unstable, decomposing easily to PtO_2 and O_2 .³⁹ Similarly, the thermodynamic stability of different oxidized forms of other noble metals significantly impact the reaction conditions, which will be discussed in detail in this paper. These metals exist in various surface states under anodic conditions, and being active oxidizing agents adds complexity to the mechanistic understanding of AcOR. As a result, understanding the role of the surface oxidation state in determining the fate of methyl radicals during acetate oxidation is pivotal.

Furthermore, AcOR can function as a proxy for electrochemical methane oxidation as breaking the first C-H bond in methane also yields surface methyl radicals.⁴¹⁻⁴³ Today, methane oxidation requires substantial positive potentials to cleave the first carbon-hydrogen (C-H) bond within methane,⁴⁴ and at these potentials, the resultant intermediates, namely methyl ($\cdot\text{CH}_3$) and methylene ($\cdot\text{CH}_2$) radicals, are prone to excessive oxidation, closing the reaction by the formation of CO_2 as the final product.^{45,46} In recent years, escalating research endeavors have been dedicated to overcoming this limitation.⁴⁷⁻⁵⁰ Therefore, for both the AcOR and methane oxidation reaction, elucidating the mechanism of how methyl radicals interact and undergo multiple coupling and deprotonation steps to give various hydrocarbon and oxygenate products can aid in guiding the design of catalysts, reactors and systems for electrochemical partial oxidation processes.

In this study, a detailed exploration of the mechanistic understanding of acetate oxidation under various operational conditions has been performed, including the effect of acetate concentration, ion flow and pH conditions. The mechanistic pathways of AcOR product formation have been investigated utilizing isotope labeling experiments. Additionally, the impact of structural oxide formation and surface chemistry on the AcOR behavior across different noble metals has been elucidated. The influence of pulsed electrolysis conditions on the resulting product profile, mainly on their time-dependent stability, has been investigated. Moreover, the stability of the product profile during larger-

scale electrolysis using a membrane-electrode assembly (MEA)-based flow cell has been analyzed and compared to that obtained on model electrodes in batch electrolysis.

RESULTS AND DISCUSSION

Time-dependent product profile and the effect of ion transport

The formation of Kolbe and Hofer-Moest products is driven by complex protonation/deprotonation and coupling/decoupling processes occurring simultaneously at the electrode surface, which influence the selectivity of products over time. Therefore, the time-dependent selectivity of AcOR products was tested using a Pt anode in a three-electrode batch cell with a 0.5 M CH₃COOK electrolyte. The effluent gas from the cell was injected into an integrated gas chromatography/mass spectrometer (GC/MS) system in 16 min intervals to assess the products. Although the results were not obtained in real-time, the measurements at consecutive intervals provide a clear representation of the evolving reaction pathway and the corresponding product selectivity trends. The time-dependent change in the product concentration profile obtained during acetate oxidation performed at 3.2 V is shown in Figure 1a. The relative concentration of products was consistent over 6 h except for ethylene and formaldehyde (Figure S1), and there were notable differences in terms of product concentration. Initially, the total concentration of the products accounted for ~ 85000 ppm after 20 min of electrolysis, which continuously degraded over time. Kolbe products such as ethylene and ethane, were the major species formed initially, while HCOH was the only oxygenate produced at a higher concentration. Although alcohols were produced, they accounted for less than 3500 ppm and among them, methanol was the major product with concentrations ranging between 1000 – 3000 ppm over 6 h of electrolysis. The product formation showed a sharp decline after 50 minutes, after which only formaldehyde was stabilized. In terms of selectivity, the relative concentration for formaldehyde increased constantly with time while that of ethylene decreased. The product changes were likely driven by the significant change in the electrolyte pH that was observed during electrolysis (Table S1). At 3.2 V, the pH shifted from 8.0 to 5.4, making the reaction environment more acidic. In addition to the pH shift, there was a significant decline in the electrolyte volume on the anode side. This led to the

question of whether the pH is the sole factor that was responsible for this decline in the activity or other reactor dynamics were playing a vital role.

During this batch of experiments, a proton exchange membrane (PEM) was used as the separator of the anodic and cathodic compartments, which allowed only positive ions to pass through it (Figure 1b). Though the migration of CH_3COOK molecules is possible under a high concentration gradient, the impact of this on the bulk pH is negligible (Note S1). Protons (H^+) and potassium ions (K^+) are the only cations present in the 0.5 M CH_3COOK solution. Since K^+ ions are the major charge carriers among the two (because of their relative concentration) and it can carry around three water molecules by electro-osmotic drag⁵¹, the sustained availability of water on the cathode side is ensured over extended periods. On the anode side, the transport of K^+ ions towards the cathode leads to a relatively higher concentration of CH_3COO^- . Ionic neutrality was maintained by water dissociation, generating OH^- and H^+ ions. The OH^- ions participate in the formation of metal oxide and OER reactions. This leads to an increase in the H^+ concentration with time at the anode, leading to a decreased pH.

Concentration-dependent investigations revealed that with an increase in the electrolyte concentration, the pH after electrolysis was slightly higher, as outlined in Table S2, resulting in a different product profile, as shown in Figure S2, for all tested acetate concentrations at 3.2 V. With an increase in acetate concentration, e.g. from 0.05 M to 0.2 M, the production of formaldehyde was significantly increased. When the acetate concentration exceeded 0.2 M, the emergence of Kolbe products and alcohols was also observed. Higher concentrations of acetate led to a broader distribution and increased concentrations of different Kolbe and oxygenate products, indicating an improved AcOR. Not only does the increased concentration improve the acetate availability at the electrode surface, the increased concentration of acetate can effectively neutralize the effect of H^+ ions by forming a $\text{CH}_3\text{COO}^-/\text{CH}_3\text{COOH}$ buffer. Consequently, elevating the acetate electrolyte concentration emerges as a potential strategy for enhancing and stabilizing the product profile for an extended time period. To test this hypothesis, acetate oxidation experiments were conducted using a 5.0 M CH_3COOK solution. Figure 1c demonstrates a more than two-fold improvement in the overall concentration of products within the first 25 min of electrolysis with 5.0 M CH_3COOK compared to 0.5 M CH_3COOK . Subsequently,

even after the initial 25 min, there was an improvement in product evolution with increasing acetate concentration. After 50 min of electrolysis, the production of formaldehyde and methanol was increased and is consistently more than 3 times higher compared to that obtained in 0.5 M CH₃COOK. Upon comparing the product distribution (Figure S1 and S3), it was observed that the selectivity for C₂H₆ and CH₃OH increased, while that for C₂H₄ initially decreased but its production was eventually stabilized at ~22 mol % of the observed products. Simultaneously, there was an enhancement in CO selectivity, coupled with a reduction in CO₂ production. No pH shift was noticed, and the volume of the electrolyte was stable. This trend suggests that higher acetate concentrations can yield more stable AcOR selectivity and activity.

Since the ion transport with a PEM led to the decrease in the pH on the anode side at low and intermediate concentration that affected the product profile, an anion exchange membrane (AEM) was employed to control the ion flow during electrolysis with 0.5 M CH₃COOK. As illustrated in Figure 1d, the use of an AEM allow for the transport of only anions from the cathode side to the anode side. Due to the water reduction reaction at the cathode, OH⁻ ions are continuously produced, leading to the presence of OH⁻ along with CH₃COO⁻ on the cathode side. As the hydroxide ions are more favorable charge carriers than acetate ions, they move through the membrane to anode side. During a 2 h electrolysis experiment, although the concentration of the products decreased when an AEM was employed, a consistent product formation was observed over an extended period, as shown in Figures 1e, f. The decline in concentration for each product was delayed in comparison to the use of a PEM (Figure 1a). Similar to the results with PEM, the primary product during electrolysis was C₂H₄, followed by C₂H₆ and HCHO, with HCHO exhibiting an increasing trend over time. It was noted that periodic overoxidation of products occurred, completely depleting Kolbe or oxygenate products approximately every 70 minutes of electrolysis (Figure 1f), indicating an increased residence time of the reaction intermediates. Though a slight variation in the pH was noticed, it was not as significant as with the PEM. The hydroxide ions that moved to the anode compartment are consumed by the OER at the anode, thereby limiting the pH change during electrolysis. Even though the use of the AEM mitigated the pH change and stabilized the product selectivity compared to the PEM, the decline in the product evolution (the actual

concentration of each product) with time still prevailed. This decline is likely due to the consumption of acetate during electrolysis. As observed previously with PEM, using a higher concentration of acetate would surpass this issue. Hence, similar to the experiments with PEM, the concentration of acetate was increased, this time to 1.5 M, and the product concentrations were increased significantly (Figure S4) with a similar trend in their relative concentrations during 1.5 h of electrolysis.

Another approach to stabilize pH is to perform electrolysis in buffer solutions. However, it is difficult to find appropriate buffers that not only have the buffering capacity, but also the needed electrochemical stability. One common buffer that was tried in this work was borate. AcOR electrolysis was conducted with 0.5 M CH_3COOK in 0.1 M borate buffer (pH 8.2) in the reacting cell with a PEM. As shown in Figure S5a, the selectivity for oxygenates increased while that of the Kolbe products was suppressed. Notably, formaldehyde exhibited consistent production exceeding 40 mol % throughout the electrolysis period, which is significantly higher than that obtained without borate buffer. Additionally, an increase in mol % of CO_2 was observed, with CO also showing an increased trend with time. The analysis of product concentrations (Figure S5c) revealed that the Kolbe formation was greatly suppressed while that of formaldehyde was unchanged compared to that without borate buffer. Despite these product changes, the buffer was not resilient to the reaction conditions, and the pH of the electrolyte did not stabilize the 3 h electrolysis; in fact, it declined to 5.4. Even increasing the borate buffer concentration to its saturation level of 0.5 M showed a similar trend of product selectivity (Figure S5b) and a pH decrease to 5.8, indicating very little buffering activity. Therefore, the addition of borate was also done with an AEM where the pH was more stable, just to probe the effect of borate as a buffer. The results are shown in Figure S6, where the trend of enhanced oxygenate selectivity and decreased Kolbe products persisted, along with increased CO_2 and CO. When the borate concentration was increased, no significant changes in product evolution were observed relative to that with the PEM (Figures S5b, d and S6b, d). An increase in alcohol concentration and the higher (mol %) for formaldehyde was evidenced from the experiments in borate buffer, which is the result of the overoxidation of alcohol products. At high positive potentials, borate forms complexes with hydroxyl groups and promotes their adsorption on the electrode surface.^{52,53} Further,

it facilitates electrochemical oxidation reactions via forming metal hydroxide and oxide bonds.⁵⁴ Thus, while the borate buffer did not stabilize the pH at such high oxidative potentials, it did influence the AcOR by altering the product selectivity, which should be studied further in the future.

Pulsed electrolysis

During electrolysis, acetate ions adsorb onto the catalyst surface and undergo oxidation through multiple electron transfer steps, involving various bond formation and dissociation events among intermediate species. The residence time of the reactants and the reaction intermediates at the electrode surface determines the extent of oxidation each molecule of acetate undergoes to form a product, thereby influencing product selectivity. For instance, shorter residence time of AcOR reactants/intermediates favor the formation of products requiring fewer electron transfer steps, such as methane, ethane, ethylene, and methanol. On the other hand, with longer residence times, an overoxidation of acetate will occur, favoring products such as formaldehyde, formate, and CO₂. As the reaction progresses, excess adsorption of reaction intermediates could block the active sites, poisoning the catalyst's surface and hinder the overall AcOR activity and the product evolution with time. This means that steady-state operation at one potential may not lead to the most stable overall product profile. Pulsed potential electrolysis, which involves applying a less anodic “resting” potential at regular intervals to interrupt steady-state time segments at high constant potential, has been implemented for various electrochemical reactions, such as CO₂ reduction, water electrolysis, methane oxidation, etc. and has shown at least some ability to modulate product selectivity⁵⁵⁻⁵⁸.

During the pulsed electrolysis cycles, when an anodic potential is applied, reactive species and intermediates are adsorbed on the anode surface and undergo oxidation reactions. When the resting potential is applied, gaseous or liquid products that may have poisoned the metal active can be removed from the surface from either desorption or reduction. In some cases, the resting potential allows for the accumulation of reactive active species that are later oxidized when the steady state potential is resumed, thereby enhancing the stability of product formation during electrolysis. In the experiments

conducted with an AEM and 1.5 M CH₃COOK on a Pt electrode, a significant enhancement of formaldehyde was observed. Perhaps this phenomenon could be attributed to the prolonged residence time of methanol on active sites of the electrode surface. Additionally, a reduction in product evolution was also noticed with prolonged electrolysis. Hence, pulsed electrolysis was implemented to understand its influence on the AcOR.

In this work, the constant high potential was 3.2 V and the resting potential was 0.5 V. The resting potential was applied every 2 hours and was 60 s in duration. The protocol was run for 7.5 hours. The AcOR products changed significantly, as shown in Figure 2 and Figure S7. The concentration (Figure S7) of the obtained products was greatly diminished for the first 2 h, the introduction of a resting potential after 2 hours resulted in a consistently stable product selectivity (Figure 2) for the rest of the electrolysis duration. Notably, the application of the resting potential did not lead to an enhancement in the selectivity for Kolbe products. Although the selectivity for C₂H₆ showed a decline, the evolution of C₂H₄ was completely suppressed. Conversely, the selectivity for Hofer-Moest products, particularly for HCHO and CH₃OH, improved initially and then remained relatively stable throughout the electrolysis duration. Furthermore, the mol % of formaldehyde was ~1.5 times that of methanol, which was 6 – 10 times during constant potential electrolysis (Figure 1e). A similar trend of stable evolution was observed for CO, while it increased for O₂. The selectivity trends suggest that the over-oxidation of some products, particularly methanol, may be controlled and a more stable over long durations with pulsed electrolysis, allow for a more desirable product selectivity to be achieved through adequate tuning of the reaction conditions and times.

Mechanistic pathways for acetate oxidation products

Given the production of Kolbe and oxygenate products, along with CH₄, CO, and CO₂ on Pt electrodes, further investigations were conducted to understand the mechanistic pathways through which the acetate is oxidized to various products. To elucidate the mechanistic pathways of acetate oxidation and the role of methyl radicals in the formation of Kolbe and Hofer-Moest products, isotope labeling experiments were

conducted by labeling carboxyl and methyl carbons of 0.5 M sodium acetate with ^{13}C in a batch cell at the Pt electrode. In the first set of experiments, ^{13}C was placed in the carboxyl functional group ($\text{CH}_3^{13}\text{COONa}$). The resulting GC-MS analysis (Figure S8) indicated that the carboxyl group is the primary source of CO_2 (Figure 3). Conversely, when the methyl carbon was labeled with ^{13}C ($^{13}\text{CH}_3\text{COONa}$), it was observed that all carbon products containing C-H bonds incorporated ^{13}C (Figure S9). These findings suggest that upon the cleavage of the C-C bond in acetate, a pivotal step in the reaction, the carbonyl intermediate departs from the anode as CO_2 and leaves activated $\cdot\text{CH}_3$ radicals bound to the electrode surface as indicated by path 3 in Figure 3. Simultaneously, surface-bound methyl radicals engage with either $\cdot\text{CH}_x$ or $\cdot\text{OH}$ radicals, leading to the Kolbe or Hofer-Moest reactions.

During the isotope labeling experiments, a range of C_1 to C_3 products, such as CO , CH_4 , CH_3OH , HCHO , HCOO^- , HCOOCH_3 , C_2H_4 , C_2H_6 , and $\text{CH}_3\text{COOCH}_3$ were identified. Based on the results, possible reaction mechanisms are proposed in Figure 3. In the initial step, acetate adsorbs on the electrode surface (path 1) via bidentate bond formation^{61,62}, followed by the breakage of the bond between the methyl and carbonyl groups, leading to the formation of CO_2 and activated $\cdot\text{CH}_3$ radicals.⁶³ The combination of two chemisorbed methyl radicals happens via the Kolbe reaction, forming C_2H_6 , as indicated by path 4 in Figure 3.¹⁷ The methyl radicals formed via path 3 can also undergo deprotonation, resulting in the adsorbed methylene ($\cdot\text{CH}_2$) radicals (path 5). Two of the $\cdot\text{CH}_2$ radicals then combine to yield C_2H_4 (path 8). On the other hand, the $\cdot\text{H}$ formed by the deprotonation of $\cdot\text{CH}_3$ radicals can either lead to H_2 (path 10) or combine with a $\cdot\text{CH}_3$ radical present in its vicinity to give CH_4 (path 9). However, CH_4 also forms by the coupling of $\cdot\text{CH}_3$ and $\cdot\text{H}$ produced by water splitting reaction (path 17). In addition to the Kolbe reaction, the $\cdot\text{CH}_3$ radicals generated during path 3 undergo Hofer-Moest reactions to give oxygenate products. For instance, coupling $\cdot\text{OH}$ and $\cdot\text{CH}_3$ radicals leads to CH_3OH , as indicated by path 6. Additionally, it can be combined with surface-adsorbed acetate ions to give $\text{CH}_3\text{COOCH}_3$. HCHO can be formed either by the oxidation of CH_3OH (path 12) or by coupling a $\cdot\text{CH}_2$ radical with $\cdot\text{O}$ (path 11).⁶⁴ The generated HCHO can further oxidize to give formate⁶⁵ that can proceed to combine with methyl radicals and generate methyl formate (paths 15, 16). In addition to the reactions discussed above, an alternative

pathway for methyl radical formation involves the condensation of acetate ions followed by the evolution of CO, as indicated by paths 13 and 14.

Next, experiments were done with H_2^{18}O and D_2O , which provided additional insights into the involvement of water in the electrolysis process. While $\text{CH}_3^{18}\text{OH}$ and $\text{C}_2\text{H}_5^{18}\text{OH}$ were detected (Figure S10), alcohols with deuterium were absent in experiments (Figure S11). This indicates that the contribution of $\cdot\text{H}$ radicals, rather than H^+ from water splitting, is significant in driving the formation of products, and oxygen from water rather than acetate is responsible for oxygenate products. At the positive potential where the electrolysis was undertaken, surface oxide formation and structural reconstruction extensively occur.⁶⁶ Furthermore, the water-splitting reaction involves the adsorption of $^*\text{OH}$ on the catalyst surface, and its conversion to structural oxygen has been reported in the literature.⁶⁷ This observation suggests that the oxygen from water in the electrolyte contributes to the formation of surface and/or structural oxide on the metal catalyst, and the formed oxide contributes to the generation of oxygenates. In addition to this, the presence of ^{13}C in CH_4 , produced during acetate electrolysis with methyl carbon labeled with ^{13}C , suggests that methane production occurs through the combination of methyl radicals with hydrogen radicals, i.e., the path 9 rather than path 17 (Figure 3). The role of surface oxidation in the AcOR is further discussed in the following section.

Linking AcOR products to the oxidation state of noble metal electrodes

Because the isotope labeling experiments suggested that structural oxides contribute to the product formation pathways, further investigations were undertaken to understand the role of the surface oxide state on the selectivity of the products over different noble metals such as Pt, Pd, and Au. Figure 4a shows the potential-dependent product distribution for each of the products during acetate electrolysis in 0.5 M CH_3COOK over a Pt anode. The mol %, yield and faradaic efficiency (Figure 4a, Table S3) values reported here are the average values obtained from six consecutive GC-MS injections. Notably, despite CO_2 constituting almost 50% of the obtained products across various applied potentials, ethylene and ethane were significantly generated, indicating a favorable Kolbe reaction. It is essential to highlight that trace amounts of alcohols,

formaldehyde, and CO were also formed in this process, which was expected given the results of the sections above.

In the context of electrocatalysis, when operating at high potentials within an aqueous environment the formation of a structural oxide is unavoidable. However, the resulting oxide can have many effects, either passivating/obstructing active sites and/or facilitating product formation. Numerous studies in the literature propose that the transition of metal oxidation states plays a pivotal role in activating methane and its conversion into alcohols.⁶⁸⁻⁷¹ Therefore, it becomes crucial to comprehend the role of surface oxides in influencing product selectivity. The structural changes that occurred on the Pt surface due to surface oxidation to PtO and PtO₂ happened *in-situ* during AcOR and were evaluated by collecting cyclic voltammograms (CVs) before and after electrolysis. Figures 4b and S12 show CVs taken before and after electrolysis at various applied potentials. Prior to electrolysis, the CV of Pt showed characteristic reduction and oxidation peaks at 0.6 V and 1.4 V, respectively. These can be attributed to the OH adsorption/desorption and, the conversion of adsorbed OH to the adsorbed O species, and the surface oxide formation.⁷² However, when the electrolysis was carried out at 2.9 V for 2 h, these peaks were shifted towards less positive potentials. This shift continued until the electrolysis was performed at 3.1 V. Conversely, when the applied potential for electrolysis was further increased, the shift was reversed, and a slight shift towards positive potentials was observed. The reason for this shift could be attributed to the shift in the pH during electrolysis (Table S1). Additionally, the intensity of the anodic peaks significantly increased. The presence of water molecules and CO (from AcOR) at the Pt surface modulate the mechanism of surface oxide formation and surface reconstruction⁷³⁻⁷⁵, which could be the reason for the observed differences in the peak positions and shapes of anodic peaks. The Pourbaix diagram of Pt in water indicates the higher surface hydration ability with Pt(OH)₂ formation occurring at 0.6 V at pH 7, transitioning to PtO₂ beyond 0.8 V, however in hydrous form. On the other hand, at applied potentials of 1.9 V and above, the formation of very thick oxide layers of hydrous PtO₂ has been reported.⁷⁴ While the formation of the PtO₃ phase at the potentials beyond 1.8 V is indicated, it is highly unstable and decomposes into PtO₂ and O₂.³⁹ This indicates that the structural oxide of the Pt is highly stable across a wide range of potentials, explaining the stable

selectivity of the products during AcOR. Considering the range of potentials at which the electrolysis was performed, the active surface of Pt will be in PtO₂ state at all the potentials applied. Together, the stable selectivity towards CO₂ and Kolbe products at all applied potentials could be attributed to the PtO₂ surface state.

The AcOR was also examined on an Au surface. As shown in Figure 4c and Table S4, the preference for Kolbe versus Hofer-Moest products was found to be dependent on the applied potential. Throughout the tested potentials, with the exception of 1.5 V, CO₂ emerged as the predominant product (>80 mol %), followed by H₂ (>10 mol %), indicating an over-oxidation of acetate. At the lowest applied potential of 1.2 V, only CO was produced. Selectivity for Kolbe products improved with an increase in potential to 1.4 V, shifting towards oxygenates as the potential was further raised to 1.5 V. The root cause for this shift was investigated again by cyclic voltammetry.

Figure 4d shows the CVs of Au recorded after each electrolysis experiment, revealing structural changes occurring on the Au surface corresponding to the applied positive potential. Positive potentials lead to the growth of Au(OH)₃, AuOOH, and Au₂O₃ oxide films on the Au surface in aqueous electrolyte^{76,77}, with their stability dependent on the potential range applied^{78,79}. DFT studies performed by Diaz-Morales et al.⁸⁰, coupled with in-situ surface-enhanced Raman spectroscopy, provide valuable insights on the surface oxidation states and their potential-dependent stability. The most common oxidation state that exists on Au at positive potentials is +3. However, the degree of surface hydration of the gold electrode, influenced by the applied potential, determines the specific oxidized form of Au(III), i.e., Au(OH)₃, AuOOH, and Au₂O₃. Following the initial adsorption of OH species onto the gold surface, Au(OH)₃ formation is facilitated at potentials beyond 1.17 V, remaining stable until 1.28 V. This process induces surface regeneration and the formation of Au islands, serving as sites for further oxidation and surface roughening.^{80,81} Within this potential range, only the formation of H₂, CO, and CO₂ was observed. Beyond 1.28 V, the AuOOH phase becomes stable until 1.54 V. Notably, within this potential range, the detection of Kolbe and Hofer-Moest products with significant selectivity was observed. At higher positive potentials, AuOOH transitions into an unstable hydrous Au₂O₃ phase, decomposing to the more stable Au₂O₃ phase.^{80,81} Furthermore, according to the Pourbaix diagram, at potentials higher than 2.4 V, Au₂O₃

converts to AuO_2 in the presence of water.³⁹ AuO_2 is a strong oxidizing agent, and easily decomposes to Au_2O_3 , releasing O_2 . The formation of Au_2O_3 and AuO_2 favors over-oxidation products, namely CO_2 and CO . Together, the results indicate that the selectivity towards Kolbe and alcohol products over Au is totally dependent on the degree of surface hydration – with AuOOH being the most desirable surface state.

Compared to Pt, Au exhibits surface hydration at more positive potentials. This behavior, coupled with the unique ability of Au to exist in multiple oxidation states, leads to the formation of various hydroxide and oxide forms. However, the hydroxides and oxides are less stable and can change within a narrow potential window. The dynamic nature of Au results in great variation of structural oxide, unlike Pt, which forms highly stable structural oxides across a broad potential range due to the limited variations in its hydroxide and oxide phases. As a result, the dynamic behavior of Au facilitates selective reaction pathways during AcOR, allowing for controlled product distribution based on the applied potential.

Next, AcOR studies were conducted on Pd surfaces to further understand the role of surface oxidation state on acetate oxidation ability. Though it belongs to the Pt group on the periodic table, the surface chemistry of Pd is significantly different than Pt as the former oxidizes readily, even to +6 valency, and possesses stronger dissolution than the latter.^{82,83} The electrochemical behavior of Pd in an acetate medium was initially assessed by CV before running any chronoamperometric experiments. The typical CV, shown in Figure 4f, shows anodic peaks at ~ 0.5 and ~ 1.3 V, corresponding to the surface oxidation of Pd to PdOH/PdO and PdOH/PdO to PdO_2 , respectively, and cathodic peaks at ~ 0 V and ~ 0.5 V related to the corresponding surface oxide reduction processes.⁸³⁻⁸⁵ It is worth noting that a CO stripping peak also appears at approximately around 0.5 V over Pd surfaces.⁸⁶ The high intensity of the CO stripping peak indicates the efficient oxidation of CH_3COO^- on the Pd surface to CO, which may eventually oxidize to CO_2 .⁸⁶ The product profile shown in Figure 4e and their yield tabulated in Table S5 indicate that CO_2 and CO were the only carbon products formed at the tested potentials apart from O_2 and H_2 , and at a highly positive potential (1.8 V) OER dominated AcOR. During the electrolysis, an excessive discoloration of the Pd electrode was noticed, indicating dissolution of the metal

and surface restructuring. The dissolution to clean Pd alters the surface state significantly, modifying the active sites.

The Pourbaix diagram of Pd³⁹ reveals that its structural oxide formation is comparable to that of Pt. At 0.6 V in water at pH 7, Pd transitions to Pd (II) oxides ($\text{Pd}(\text{OH})_2/\text{PdO}\cdot\text{H}_2\text{O}$). As the potential increases to 1.2 V, Pd(IV) oxides ($\text{Pd}(\text{OH})_4/\text{PdO}_2$) become prevalent. However, $\text{Pd}(\text{OH})_4$ is highly unstable, decomposing readily to release oxygen and acts as a strong oxidizing agent. PdO_3 can form above 1.8 V, but is very unstable at $\text{pH} \leq 7$. Experimentally it is reported that the surface of Pd starts oxidizing to Pd (II) hydroxides and oxides at potentials ranging between 0.6V and 0.75 V, and the potential limit to form the first monolayer of Pd(II) oxide is in the range of 1.4 V – 1.5 V.⁸³ On the other hand, the onset of Pd(IV) oxide (PdO_2) happens beyond 1.2 V, in agreement with the Pourbaix diagram. At the potentials greater than the onset of the oxygen evolution reaction, thick PdO_2 layers (β -Pd oxides) are generated.⁸³ Taken together, the presence of hydrous Pd(II) oxides ($\text{PdOH}/\text{PdO}\cdot\text{H}_2\text{O}$) would favor the acetate oxidation reaction, while the multilayered Pd(VI) oxides (PdO_2/β -Pd oxides) and the dissolution to clean Pd alter the reaction pathway favoring oxygen evolution over acetate oxidation.

Similar to Pt, Pd possesses limited stable structural oxide phases/hydrated forms, but exhibits significantly greater surface modifications at lower potentials compared to Pt. Also unlike Pt, the hydroxide and oxide phases of Pd co-exist for a given Pd valency. Despite the ability of Pd to exist in multiple oxidation states, it does not exhibit similar dynamic changes in the structural oxide phases as was seen in Au. Additionally, the stability of Pd oxides with higher valency is less than desirable. These differences in the types of structural oxides and their availability to participate in the catalytic reaction are reflected in the product distribution and the limited number of chemical species that were formed during AcOR.

Given the notable impact of electrolyte concentration and membrane type on product evolution in the results shown above, a potential-dependent product survey was conducted with Pt, Au and Pd using a 1.5 M CH_3COOK electrolyte with an AEM. As shown in Figure 5a, regardless of the applied potential, OER dominated over AcOR, with relative concentration of ~50 mol %. Furthermore, a significant shift in product selectivity was observed, transitioning from Kolbe products to oxygenates. The relative concentration of

ethane was consistent with the results discussed above, and the ethylene production was greatly suppressed. Again, there was a significant increase in the formaldehyde observed, with mol % ranging between 20% and 30%, depending on the applied potential (Figures 5a and S13, Table S3), thus competing with the ethane production. There was also a drastic reduction in the mol % of CO₂, dropping from approximately 45% to less than 5%, suggesting effective control over the overoxidation of products in the changed conditions. With the use of an AEM, the accessibility of OH⁻ ions at the anode will increase due to their transport from the cathode side, resulting in a control over pH change during electrolysis. This contributes to the stabilization of oxide phase of the catalyst, as discussed earlier based on the Pourbaix diagrams, and the availability of surface oxygen species, contributing to the enhanced OER and oxygenate selectivity as discussed by path 11 in Figure 3.

On Au in 1.5 M CH₃COOK electrolyte, a limited product profile was observed (Figures 5b and S14, Table S4). While a small amount of ethane was produced at 1.3 - 1.4 V, ethylene was not detected. A trace amount of methanol was detected only at 1.8 V, while ethanol was completely absent. Formaldehyde, an over-oxidation product, was formed at the potentials where Kolbe and alcohols were observed with a PEM (1.4-1.5 V). Improved formaldehyde production was also observed with a Pt electrode. The availability of more OH⁻ ions at the electrode may facilitate a rapid bonding of methyl radicals with OH species as shown by path 6 in Figure 3 to give methanol followed by a further oxidation to formaldehyde. Furthermore, a stronger stabilization of these intermediates resulted in rapid deprotonation, thus forming formaldehyde and hydrogen. Conversely, no substantial difference was observed in terms of type of products obtained with the Pd electrode (Figures 4e, 5c, and S15, Table S5). CO₂ and O₂ were the major products produced irrespective of the applied potential. However, in contrast to that with a PEM, OER was dominant over CO₂ with the use of AEM except at 1.7 V. Though produced in very small quantities, formaldehyde was present at all applied potentials in contrast to the CO produced with a PEM. This is in agreement with the observations noticed at Pt and Au electrodes, where also formaldehyde dominated among the AcOR products other than CO₂.

AcOR products in an operating flow cell

Flow cells utilizing a membrane electrode assembly (MEA) have long been investigated within the realm of electrocatalysis to address and overcome mass transport limitations.^{87,88} Consequently, this approach enables higher current densities and increased product formation, which could allow such technologies to be scaled. To evaluate the AcOR performance under a zero-gap design, a flow cell electrolyzer (Figure 6a) equipped with a Pt/C catalyst-coated gas diffusion layer (GDL) anode, PtNi catalyst-coated GDL cathode, and a quaternized poly(norbornene) AEM was employed. As illustrated in Figure 6a, the anolyte flow field was fed with 1.5 M CH₃COOK at 2 mL/min, with the outlet connected to the GC-MS. On the cathode side, the inlet was closed, and the outlet of the flow field was left open to allow the H₂ gas produced at the cathode to escape. During electrolysis, the electrolyte diffuses through the anode-GDL, and the acetate ions adsorb and undergo oxidation on the Pt/C catalyst. The oxidation products then diffuse back into the anolyte flow channel. Water from the electrolyte diffuses through the membrane and undergoes water reduction at the cathode. The H₂ generated at the cathode will diffuse through the cathode-GDL into the catholyte flow channel. The OH⁻ ions produced during HER at the cathode transport through the AEM membrane and contribute to the oxidation process occurring at the anode, as discussed earlier.

In the electrolyzer experiments, Pt/C catalysts were selected because Pt exhibited a stable selectivity over a wide range of potentials in the batch cell. The polarization curve recorded using an MEA set-up is shown in Figure S16, revealing the operation of the cell at high current densities at the potentials where the electrolysis was undertaken using a batch cell. As expected, higher current densities were observed in the flow cell than the batch cell (Figure S17a) and the Pt catalyst demonstrated similar products selectivity (except for methanol) to the batch cell operating at 3.5 V (Figure 6b). Furthermore, a superior HCHO selectivity was also observed among the oxidized products, resulting from the oxidation of methanol. Notably, the overall FE increased, with CO₂ contributing roughly 80%, suggesting extensive acetate overoxidation under high mass transport conditions enabled by the MEA flow cell. However, it is also worth noting that carbon corrosion likely contributed at least some fraction of the measured CO₂, which was confirmed in cells assembled with C black in the catalyst layer and no Pt (polarization and

galvanostatic operation shown in Figure S18, brief discussion in Note S2). Also positive, the single pass conversion was calculated to be 14%, without any optimization applying chemical reaction engineering principles. These observations indicate the possibility of scaling up AcOR to meet industrial requirements, however, with further optimization.

Conclusions

A comprehensive evaluation of electrochemical acetate oxidation has been done, providing valuable insights into the underlying mechanisms and product distribution – supported by a number of electrochemical experiments and isotope labeling studies. Time dependent analysis of the AcOR product distribution at a Pt anode revealed a significant variation in Kolbe product formation with time coupled with a gradual increase in formaldehyde. A dynamic shift in electrolyte pH and instability of product selectivity with time were observed during anodic electrolysis when using a PEM separator, which was avoided when using an AEM – showing that control over ion transport is important in controlling the mechanism and product stability. Concentration-dependent studies showed that buffering the solution with excess reactant can also stabilize the product profile. Introducing additive ions (e.g., borate) can also influence the product profile, though borate was not an adequate buffer. Introducing resting potentials at designated intervals via pulsed electrolysis was also effective in improving and stabilizing the product profile and selectivity over a long duration. The surface oxidation state was shown to have a significant influence over the product profile across different noble metals (Pt, Au, Pd). Finally, a Pt catalyst was used in a flow cell electrolyzer, showing selectivity towards AcOR products that was similar to smaller batch cell experiments, suggesting the feasibility for future scale up.

EXPERIMENTAL PROCEDURES

Materials

Platinum (99.9%, 0.1 mm thick, product number (P/N): 11509), gold (99.9%, 0.1 mm thick, P/N: 00132) and palladium (99.9%, 0.1 mm thick, P/N: 11515) foils were purchased from Alfa Aesar. Platinum foil was thermally cleaned by repeated heating with

a butane torch, followed by rapid immersion in DI water before each electrolysis experiment. Gold foil was washed with water, while palladium foil was wiped with 0.1M nitric acid and rinsed with DI water before each experiment. Nafion® - 212 proton exchange membrane purchased from Thermo Scientific. A-201 anion exchange membrane was obtained from Tokuyama. The quaternized poly(norbornene) GT75-5 anion exchange membrane, GT25 and GT69 ionomers were supplied by the Kohl group at the Georgia Institute of Technology; details about the preparation of these polymers can be found elsewhere.^{89,90} Briefly, the numbering system details the fraction of functionalized monomer and the degree of crosslinking. GT-75-5 membranes have 75 mol% of functionalized monomer and 5 mol% cross-linker (N,N,N',N'-tetramethyl-1,6-hexanediamine) relative to the mol% of the halogenated monomers in the polymer. GT25 and GT69 ionomers have 25 mol % and 69 mol% functionalized monomer, respectively, and no crosslinker. 5% PTFE coated Toray-60 carbon paper (Lot: 4655-T060) was purchased from Fuel Cell store. Pt/C (40 wt%, Lot: Z06I033) was purchased from Thermo Scientific. PtNi catalyst was purchased from Pajarito powder (Lot: 0020-0). Potassium acetate (CH₃COOK, 99.0%), potassium nitrate (KNO₃, 100.3%), and boric acid (H₃BO₃, 99.5%) were purchased from Fisher chemical. Potassium carbonate (K₂CO₃, 99.0%) was purchased from Alfa Aesar. Potassium hydroxide (KOH, 85.5%) was purchased from Macron Fine Chemicals. Deuterium oxide (D₂O, 99.8 atom % D) was purchased from Acros Organics. Acetone (99.5%) was purchased from VWR Chemicals. CH₃¹³COONa (99.0 atom % ¹³C) and ¹³CH₃COONa (99.0 atom % ¹³C) were purchased from Aldrich. All chemicals were used as received. Ultrapure deionized water (18.2 MΩ-cm) was obtained from a Millipore Milli-Q® Integral 5 water purification system, which was utilized to prepare all of the aqueous solutions.

Electrochemical instrumentation and methods

Electrochemical measurements were made in two cell types. The first was a two-compartment, air-tight electrochemical cell consisting of three electrodes (working electrode, Pt counter electrode, and Ag/AgCl_{sat.KCl} reference electrode). The design of the cell is shown in Figure S19. The working electrode had a surface area of 4.5 cm² (1.5 cm X 3.0 cm). The two 10 mL volume compartments were separated by a membrane and

filled with 8 mL of CH₃COOK electrolyte of various concentrations. He (5.0 UHP grade, Linde) gas was used as a carrier gas and was continuously passed through the anolyte with a flow rate of 10 mL min⁻¹ throughout the experiments. The He stream was fed directly to a customized, integrated gas chromatograph-mass spectrometer (GC-MS) system with an Agilent Technologies 7890B GC system and 5977B MSD. An Autolab PGSTA302N potentiostat was used to record all electrochemical measurements, which were conducted at 23 ± 2 °C. Cyclic voltammograms (CVs) were recorded at a scan rate of 100 mV s⁻¹ in the absence of He gas flow. Chronoamperometric electrolysis was done at several potentials for a period of 1 h unless otherwise stated. Pulsed electrolysis was carried out with the same reaction conditions for a period of 7.5 h where at selected intervals (typically every 2 h), a low oxidation potential of 0.5 V was applied for 60 seconds, followed by a higher oxidation potential of 3.2 V. Applied potentials measured vs Ag/AgCl were converted to RHE using the formula in Equation 2.

$$E_{RHE} = E_{Ag/AgCl} + 0.199 (V) + 0.0586 (V) * pH \text{ (at } 23 \pm 2 \text{ °C)} \quad (2)$$

The pH of the electrolyte was measured before and after electrolysis using a Mettler-Toledo SevenGo Duo pro pH/Ion/Cond meter equipped with an InLab® Expert Pro-ISM probe.

The second cell type was a MEA-based flow cell. The catholyte and anolyte flow fields were made from graphite and stainless steel, respectively, and both had a single serpentine flow pattern. The MEA consisted of anode and cathode gas diffusion electrodes separated by an anion exchange membrane (GT75-5). The electrode active area was 5 cm². The 1.5 M CH₃COOK electrolyte was constantly pumped through the flow field at a flow rate of 2 mL min⁻¹. Chronopotentiometric electrolysis was done at an applied current density of 50 mA cm⁻² for 2 h. Polarization curves were recorded before and after electrolysis at a scan rate of 50 mA s⁻¹. All the experiments were conducted at 23 ± 2 °C.

Membrane pretreatment

Nafion-212 membranes were stored in DI water and used without any pretreatment. A-201 membranes were soaked in 1.0 M KOH for at least 30 min before

use. GT-75-5 membranes were soaked in 50 wt% aqueous trimethylamine solution for 24 h, followed by soaking in 1.0 M KOH for 30 min.

Gas diffusion electrodes

GT-25 and GT-69 ionomers were used in the catalyst inks for the anode and cathode, respectively. To prepare the catalyst inks, the ionomer was first wetted by adding 1 mL of DI water and allowing it to hydrate for ~30 min. The resulting swollen polymer was mortared into a fine powder, and the catalyst powder (40 wt% Pt/C for the anode and PtNi for the cathode) was added and mixed in thoroughly by grinding. An additional 5 mL of DI was added at different stages to the obtained catalyst-ionomer mixture in order to keep them wet and mortared further for 10 minutes. The liquids and solids were transferred into a centrifuge tube along with isopropyl alcohol of volume 9 times to that of water used to prepare the catalyst-ionomer mixture. The final ink was created by ultrasonication in an ice bath for 60 min. Lastly, the inks were spray coated onto a gas diffusion layer substrate (Toray-60 carbon paper, 5 % wet proof) with a targeted loading of 1.4 mg cm⁻² for the anode and 1.0 mg cm⁻² for the cathode.

Product quantification

The products generated during acetate oxidation-reduction were identified and quantified using an integrated gas chromatography (Agilent 7890B) - mass spectroscopy (Agilent 5977A MSD) system equipped with a column of length 30 m. A thermal conductivity detector (TCD) was utilized to detect H₂, CO₂, O₂, and CH₄, while CO was detected using a pulsed discharge helium ionization detector (PDHID). Hydrocarbons and oxygenates such as CH₄, C₂H₆, C₂H₄, CH₃OH, C₂H₅OH and HCHO were detected using a mass selective detector (MSD). The detection method was programmed such that the total retention time was 15 min. For each electrolysis experiment, a series of sample injections were made at successive 16 min intervals. The obtained data for each injection was quantified by using the calibrations obtained with known gas standards. The reported values were the average of the quantification values obtained from the series of injections.

Following quantification, the relative concentration (mol %) of the products was calculated using Equation 3:

$$\text{Relative concentration of product } i (\%) = \frac{[i]}{\sum[\text{products}]} * 100 \quad (3)$$

where $[i]$ is the concentration of product i in ppm and $\sum[\text{products}]$ is the sum of concentrations of all the obtained products. The faradaic efficiency of the obtained products was calculated using Equation 4:

$$\eta_i = \frac{n * N * F}{Q} * 100 \quad (4)$$

where, η_i is the faradaic efficiency of the product i , n is the moles of electrons transferred for each mol in producing species i , N is the number of moles of the product obtained from the ppm concentrations quantified using GC-MS, Q is the total coulombs of charge passed during electrolysis and F is the faraday's constant. Single pass conversion efficiency was calculated using Equation 5:

$$\text{Single pass conversion efficiency (\%)} = \frac{\text{moles of acetate oxidised}}{\text{moles of acetate at the inlet}} * 100 \quad (5)$$

RESOURCE AVAILABILITY

Lead contact

Requests for further information and resources should be directed to and will be fulfilled by the lead contact, Prof. William E. Mustain (mustainw@mailbox.sc.edu).

Materials availability

This study did not generate new unique reagents.

Code and data availability

Any additional information required to reanalyze the data reported in this paper is available from the lead contact upon request.

SUPPLEMENTAL INFORMATION

Supplemental Information can be found online at.

The supplemental information includes Figures S1-S19, Notes S1 and S2 and Tables S1-S5.

ACKNOWLEDGMENTS

This work was supported by the National Science Foundation under Award Number 2025709. The authors acknowledge Prof. Paul A. Kohl (Georgia Institute of Technology) for providing the membranes and ionomers.

AUTHOR CONTRIBUTIONS

Conceptualization, supervision, project administration, and funding acquisition: W.E.M; methodology and data curation: V.S.S.M., H.S., X.P., E.F., M.E. and I.S.; formal analysis and investigation: V.S.S.M., H.S. and X.P.; visualization: V.S.S.M. and I.S., writing (original draft): H.S. and V.S.S.M., writing (review and editing): V.S.S.M. and W.E.M.

DECLARATION OF INTEREST

The authors declare no competing interests.

REFERENCES

1. Xia, R., Overa, S., and Jiao, F. (2022). Emerging Electrochemical Processes to Decarbonize the Chemical Industry. *JACS Au* 2, 1054-1070. <https://doi.org/10.1021/jacsau.2c00138>.
2. Li, R., Xiang, K., Peng, Z., Zou, Y., and Wang, S. (2021). Recent Advances on Electrolysis for Simultaneous Generation of Valuable Chemicals at both Anode and Cathode. *Adv. Energy Mater.* 11, 2102292. <https://doi.org/10.1002/aenm.202102292>.
3. Sen, K.Y., and Baidurah, S. (2021). Renewable biomass feedstocks for production of sustainable biodegradable polymer. *Curr. Opin. Green Sustainable Chem.* 27, 100412. <https://doi.org/10.1016/j.cogsc.2020.100412>.

4. Palkovits, R. (2018). Sustainable Carbon Sources and Renewable Energy: Challenges and Opportunities at the Interface of Catalysis and Reaction Engineering. *Chem. Ing. Tech.* 90, 1699-1708. <https://doi.org/10.1002/cite.201800042>.
5. Subbarao, P.M.V., D' Silva, T.C., Adlak, K., Kumar, S., Chandra, R., and Vijay, V.K. (2023). Anaerobic digestion as a sustainable technology for efficiently utilizing biomass in the context of carbon neutrality and circular economy. *Environ. Res.* 234, 116286. <https://doi.org/10.1016/j.envres.2023.116286>.
6. Pan, S.-Y., Tsai, C.-Y., Liu, C.-W., Wang, S.-W., Kim, H., and Fan, C. (2021). Anaerobic co-digestion of agricultural wastes toward circular bioeconomy. *iScience* 24, 102704. <https://doi.org/10.1016/j.isci.2021.102704>.
7. Pan, X., Zhao, L., Li, C., Angelidaki, I., Lv, N., Ning, J., Cai, G., and Zhu, G. (2021). Deep insights into the network of acetate metabolism in anaerobic digestion: focusing on syntrophic acetate oxidation and homoacetogenesis. *Water Res.* 190, 116774. <https://doi.org/10.1016/j.watres.2020.116774>.
8. Karakashev, D., Batstone Damien, J., Trably, E., and Angelidaki, I. (2006). Acetate Oxidation Is the Dominant Methanogenic Pathway from Acetate in the Absence of Methanosaetaceae. *Appl. Environ. Microbiol.* 72, 5138-5141. <https://doi.org/10.1128/AEM.00489-06>.
9. Westerholm, M., Moestedt, J., and Schnürer, A. (2016). Biogas production through syntrophic acetate oxidation and deliberate operating strategies for improved digester performance. *Appl. Energy* 179, 124-135. <https://doi.org/10.1016/j.apenergy.2016.06.061>.
10. Backes, M.J., Lukaski, A.C., and Muggli, D.S. (2005). Active sites and effects of H₂O and temperature on the photocatalytic oxidation of ¹³C-acetic acid on TiO₂. *Appl. Catal. B.* 61, 21-35. <https://doi.org/10.1016/j.apcatb.2005.03.012>.
11. Belhadj, H., Melchers, S., Robertson, P.K.J., and Bahnemann, D.W. (2016). Pathways of the photocatalytic reaction of acetate in H₂O and D₂O: A combined EPR and ATR-FTIR study. *J. Catal.* 344, 831-840. <https://doi.org/10.1016/j.jcat.2016.08.006>.
12. Hamid, S., Ivanova, I., Jeon, T.H., Dillert, R., Choi, W., and Bahnemann, D.W. (2017). Photocatalytic conversion of acetate into molecular hydrogen and hydrocarbons over Pt/TiO₂: pH dependent formation of Kolbe and Hofer-Moest products. *J. Catal.* 349, 128-135. <https://doi.org/10.1016/j.jcat.2017.02.033>.
13. Liu, S., Govindarajan, N., Prats, H., and Chan, K. (2022). Understanding the reaction mechanism of Kolbe electrolysis on Pt anodes. *Chem Catal.* 2, 1100-1113. <https://doi.org/10.1016/j.chechat.2022.02.014>.
14. Faraday, M. (1834). Siebente Reihe von Experimental-Untersuchungen über Elektricität. *Ann. Phys.* 109, 433-451. <https://doi.org/10.1002/andp.18341092307>.
15. Zersetzung der Valeriansäure durch den elektrischen Strom. (1848). Justus Liebigs Ann. Chem. 64, 339-341. <https://doi.org/10.1002/jlac.18480640346>.
16. Kolbe, H. (1849). Untersuchungen über die Elektrolyse organischer Verbindungen. Justus Liebigs Ann. Chem. 69, 257-294. <https://doi.org/10.1002/jlac.18490690302>.
17. Vlijh, A.K., and Conway, B.E. (1967). Electrode Kinetic Aspects of the Kolbe Reaction. *Chem. Rev.* 67, 623-664. 10.1021/cr60250a003.

18. Shukla, S.N., and Walker, O.J. (1932). Anode phenomena in the electrolysis of potassium acetate. Part III. Formation of methane. *Transactions of the Faraday Society* 28, 457-462. <https://doi.org/10.1039/TF9322800457>.
19. Shukla, S.N., and Walker, O.J. (1931). Formation of methane during the electrolysis of potassium acetate, and the mechanism of Kolbe's electro-synthesis. *Trans. Faraday Soc.* 27, 35-40. <https://doi.org/10.1039/TF9312700035>.
20. Fioshin, M.Y., and Vasil'ev, Y.B. (1963). Kinetics of anodic and chemical reactions in Kolbe's electrosynthesis. *Bull. Acad. Sci. USSR, Div. Chem. Sci.* 12, 393-400. <https://doi.org/10.1007/BF00844388>.
21. Fleischmann, M., Mansfield, J.R., and Wynne-Jones, L. (1965). The anodic oxidation of aqueous solutions of acetate ions at smooth platinum electrodes: Part II. The non-steady state of the kolbe synthesis of ethane. *J. Electroanal. Chem.* (1959) 10, 522-537. [https://doi.org/10.1016/0022-0728\(65\)80053-5](https://doi.org/10.1016/0022-0728(65)80053-5).
22. Peng, X., Omasta, T., Zhao, X., and Mustain, W.E. (2018). (Invited) Electrochemical Pathways for Electrochemical Oxidation of Acetic Acid. *ECS Trans.* 85, 29. <https://doi.org/10.1149/08510.0029ecst>.
23. Ross, S.D., Finkelstein, M., and Petersen, R.C. (1964). The Electrochemical Oxidation of Acetic Acid in the Presence of Aromatic Hydrocarbons. *J. Am. Chem. Soc.* 86, 4139-4143. <https://doi.org/10.1021/ja01073a046>.
24. Barbier, J., Delanoë, F., Jabouille, F., Duprez, D., Blanchard, G., and Isnard, P. (1998). Total oxidation of acetic acid in aqueous solutions over noble metal catalysts. *J.Catal.* 177, 378-385. <https://doi.org/10.1006/jcat.1998.2113>.
25. Kunugi, T. (1953). Electrolytic Oxidation of Salts of Aliphatic Acids by the Hofer—Moest Reaction. I. Formation of Methanol from Sodium Acetate. *J. Am. Chem. Soc.* 75, 1597-1599. <https://doi.org/10.1021/ja01103a024>.
26. Qiu, Y., Lopez-Ruiz, J.A., Sanyal, U., Andrews, E., Gutiérrez, O.Y., and Holladay, J.D. (2020). Anodic electrocatalytic conversion of carboxylic acids on thin films of RuO₂, IrO₂, and Pt. *Appl. Catal. B.* 277, 119277. <https://doi.org/10.1016/j.apcatb.2020.119277>.
27. Qiu, Y., Lopez-Ruiz, J.A., Zhu, G., Engelhard, M.H., Gutiérrez, O.Y., and Holladay, J.D. (2022). Electrocatalytic decarboxylation of carboxylic acids over RuO₂ and Pt nanoparticles. *Appl. Catal. B.* 305, 121060. <https://doi.org/10.1016/j.apcatb.2021.121060>.
28. Zhang, Y., Liu, G., and Wu, J. (2018). Electrochemical conversion of palmitic acid via Kolbe electrolysis for synthesis of n-triacontane. *J. Electroanal. Chem.* 822, 73-80. <https://doi.org/10.1016/j.jelechem.2018.05.018>.
29. Neubert, K., Schmidt, M., and Harnisch, F. (2021). Platinized Titanium as Alternative Cost-Effective Anode for Efficient Kolbe Electrolysis in Aqueous Electrolyte Solutions. *ChemSusChem* 14, 3097-3109. <https://doi.org/10.1002/cssc.202100854>.
30. Yuan, G., Wu, C., Zeng, G., Niu, X., Shen, G., Wang, L., Zhang, X., Luque, R., and Wang, Q. (2020). Kolbe Electrolysis of Biomass-Derived Fatty Acids Over Pt Nanocrystals in an Electrochemical Cell. *ChemCatChem* 12, 642-648. <https://doi.org/10.1002/cctc.201901443>.
31. Andreev, V.N., Grinberg, V.A., Dedov, A.G., Loktev, A.S., Moiseev, I.I., and Tsividze, A.Y. (2013). Electrocatalytic biomass conversion into petrochemicals.

Review. Prot. Met. Phys. Chem. Surf. 49, 32-39. <https://doi.org/10.1134/S2070205113010024>.

32. Mosali, V.S.S., Bond, A.M., and Zhang, J. (2022). Alloying strategies for tuning product selectivity during electrochemical CO₂ reduction over Cu. *Nanoscale* 14, 15560-15585. <https://doi.org/10.1039/D2NR03539A>.

33. Jin, S., Hao, Z., Zhang, K., Yan, Z., and Chen, J. (2021). Advances and Challenges for the Electrochemical Reduction of CO₂ to CO: From Fundamentals to Industrialization. *Angew. Chem. Int. Ed.* 60, 20627-20648. <https://doi.org/10.1002/anie.202101818>.

34. Cui, X., Tang, C., and Zhang, Q. (2018). A Review of Electrocatalytic Reduction of Dinitrogen to Ammonia under Ambient Conditions. *Adv. Energy Mater.* 8, 1800369. <https://doi.org/10.1002/aenm.201800369>.

35. Paul, S., Adalder, A., and Ghorai, U.K. (2023). Progress of electrocatalytic urea synthesis: strategic design, reactor engineering, mechanistic details and techno-commercial study. *Mater. Chem. Front.* 7, 3820-3854. <https://doi.org/10.1039/D3QM00433C>.

36. Overa, S., Crandall, B.S., Shrimant, B., Tian, D., Ko, B.H., Shin, H., Bae, C., and Jiao, F. (2022). Enhancing acetate selectivity by coupling anodic oxidation to carbon monoxide electroreduction. *Nat. Catal.* 5, 738-745. <https://doi.org/10.1038/s41929-022-00828-w>.

37. Wu, D., Jiao, F., and Lu, Q. (2022). Progress and Understanding of CO₂/CO Electroreduction in Flow Electrolyzers. *ACS Catal.* 12, 12993-13020. <https://doi.org/10.1021/acscatal.2c03348>.

38. Nordkamp, M.O., Mei, B., Venderbosch, R., and Mul, G. (2022). Study on the Effect of Electrolyte pH during Kolbe Electrolysis of Acetic Acid on Pt Anodes. *ChemCatChem* 14, e202200438. <https://doi.org/10.1002/cctc.202200438>.

39. Pourbaix, M. (1966). *Atlas of Electrochemical Equilibria in Aqueous Solutions*. NACE.

40. Colombo, C., Oates, C.J., Monhemius, A.J., and Plant, J.A. (2008). Complexation of platinum, palladium and rhodium with inorganic ligands in the environment. *Geochem.: Explor., Environ., Anal.* 8, 91-101. <https://doi.org/10.1144/1467-7873/07-151>.

41. Campbell, K.D., Morales, E., and Lunsford, J.H. (1987). Gas-phase coupling of methyl radicals during the catalytic partial oxidation of methane. *J. Am. Chem. Soc.* 109, 7900-7901. <https://doi.org/10.1021/ja00259a059>.

42. Horn, R., and Schlögl, R. (2015). Methane Activation by Heterogeneous Catalysis. *Catal. Lett.* 145, 23-39. <https://doi.org/10.1007/s10562-014-1417-z>.

43. Kapałka, A., Lanova, B., Baltruschat, H., Fóti, G., and Comninellis, C. (2008). DEMS Study of the Acetic Acid Oxidation on Boron-Doped Diamond Electrode. *J. Electrochem. Soc.* 155, E96. <https://doi.org/10.1149/1.2917287>.

44. Tang, P., Zhu, Q., Wu, Z., and Ma, D. (2014). Methane activation: the past and future. *Energy Environ. Sci.* 7, 2580-2591. <https://doi.org/10.1039/C4EE00604F>.

45. Adebajo, M.O. (2007). Green chemistry perspectives of methane conversion via oxidative methylation of aromatics over zeolite catalysts. *Green Chem.* 9, 526-539. <https://doi.org/10.1039/B614281H>.

46. Bagherzadeh Mostaghimi, A.H., Al-Attas, T.A., Kibria, M.G., and Siahrostami, S. (2020). A review on electrocatalytic oxidation of methane to oxygenates. *J. Mater. Chem. A* 8, 15575-15590. <https://doi.org/10.1039/D0TA03758C>.

47. Tomita, A., Nakajima, J., and Hibino, T. (2008). Direct Oxidation of Methane to Methanol at Low Temperature and Pressure in an Electrochemical Fuel Cell. *Angew. Chem. Int. Ed.* 47, 1462-1464. <https://doi.org/10.1002/anie.200703928>.

48. O'Reilly, M.E., Kim, R.S., Oh, S., and Surendranath, Y. (2017). Catalytic Methane Monofunctionalization by an Electrogenerated High-Valent Pd Intermediate. *ACS Centr. Sci.* 3, 1174-1179. <https://doi.org/10.1021/acscentsci.7b00342>.

49. Oh, C., Kim, J., Hwang, Y.J., Ma, M., and Park, J.H. (2021). Electrocatalytic methane oxidation on Co₃O₄- incorporated ZrO₂ nanotube powder. *Appl. Catal. B* 283, 119653. <https://doi.org/10.1016/j.apcatb.2020.119653>.

50. Kim, J., Kim, Y.J., Ferree, M., Gunduz, S., Co, A.C., Kim, M., and Ozkan, U.S. (2023). In-situ exsolution of bimetallic CoFe nanoparticles on (La,Sr)FeO₃ perovskite: Its effect on electrocatalytic oxidative coupling of methane. *Appl. Catal. B* 321, 122026. <https://doi.org/10.1016/j.apcatb.2022.122026>.

51. Xu, F., Leclerc, S., Stommelen, D., Perrin, J.-C., Retournard, A., and Canet, D. (2017). Study of electro-osmotic drag coefficients in Nafion membrane in acid, sodium and potassium forms by electrophoresis NMR. *J. Membr. Sci.* 536, 116-122. <https://doi.org/10.1016/j.memsci.2017.04.067>.

52. Koul, A., Chandra, S., and Schuhmann, W. (2024). Selective lactic acid synthesis via ethylene glycol electrooxidation in borate buffer. *Chem. Commun.* 60, 7902-7905. <https://doi.org/10.1039/D4CC02556C>.

53. Tran, G.-S., Chen, C.-J., Maeda, S., Chikami, S., Hayashi, T., and Chiang, C.-Y. (2024). Tuning selectivity toward three-carbon product of glycerol electrooxidation in borate buffer through manipulating borate/glycerol molar ratio. *J. Catal.* 438, 115715. <https://doi.org/10.1016/j.jcat.2024.115715>.

54. Cui, L., Zhang, W., Zheng, R., and Liu, J. (2020). Electrocatalysts Based on Transition Metal Borides and Borates for the Oxygen Evolution Reaction. *Chem. Eur. J.* 26, 11661-11672. <https://doi.org/10.1002/chem.202000880>.

55. Hori, Y., Kikuchi, K., and Suzuki, S. (1985). "Production of CO and CH₄ in electrochemical reduction of CO₂ at metal electrodes in aqueous hydrogencarbonate solution". *Chem. Lett.* 14, 1695. <https://doi.org/10.1246/cl.1985.1695>.

56. Nguyen, T.N., Chen, Z., Zeraati, A.S., Shiran, H.S., Sadaf, S.M., Kibria, M.G., Sargent, E.H., and Dinh, C.-T. (2022). Catalyst Regeneration via Chemical Oxidation Enables Long-Term Electrochemical Carbon Dioxide Reduction. *J. Am. Chem. Soc.* 144, 13254-13265. <https://doi.org/10.1021/jacs.2c04081>.

57. Rocha, F., de Radiguès, Q., Thunis, G., and Proost, J. (2021). Pulsed water electrolysis: A review. *Electrochim. Acta* 377, 138052. <https://doi.org/10.1016/j.electacta.2021.138052>.

58. Sustersic, M.G., Córdova O, R., Triaca, W.E., and Arvía, A.J. (1980). The Electrosorption of Methane and Its Potentiodynamic Electrooxidation on Platinized Platinum. *J. Electrochem. Soc.* 127, 1242. <https://doi.org/10.1149/1.2129863>.

59. Yusuf, A., Snape, C., He, J., Xu, H., Liu, C., Zhao, M., Chen, G.Z., Tang, B., Wang, C., Wang, J., and Behera, S.N. (2017). Advances on transition metal oxides

catalysts for formaldehyde oxidation: A review. *Catal. Rev.* 59, 189-233. <https://doi.org/10.1080/01614940.2017.1342476>.

60. Wang, J., Zhang, B., Guo, W., Wang, L., Chen, J., Pan, H., and Sun, W. (2023). Toward Electrocatalytic Methanol Oxidation Reaction: Longstanding Debates and Emerging Catalysts. *Adv. Mater.* 35, 2211099. <https://doi.org/10.1002/adma.202211099>.

61. Pei, Z.F., and Ponec, V. (1996). On the intermediates of the acetic acid reactions on oxides: an IR study. *Appl. Surf. Sci.* 103, 171-182. [https://doi.org/10.1016/0169-4332\(96\)00453-9](https://doi.org/10.1016/0169-4332(96)00453-9).

62. Ezeonu, L., Tang, Z., Qi, Y., Huo, F., Zheng, Y., Koel, B.E., and Podkolzin, S.G. (2023). Adsorption, surface reactions and hydrodeoxygenation of acetic acid on platinum and nickel catalysts. *J. Catal.* 418, 190-202. <https://doi.org/10.1016/j.jcat.2023.01.013>.

63. Holzhäuser, F.J., Mensah, J.B., and Palkovits, R. (2020). (Non-)Kolbe electrolysis in biomass valorization – a discussion of potential applications. *Green Chem.* 22, 286-301. <https://doi.org/10.1039/C9GC03264A>.

64. De Bie, C., van Dijk, J., and Bogaerts, A. (2015). The Dominant Pathways for the Conversion of Methane into Oxygenates and Syngas in an Atmospheric Pressure Dielectric Barrier Discharge. *J. Phys. Chem. C* 119, 22331-22350. <https://doi.org/10.1021/acs.jpcc.5b06515>.

65. Batista, E.A., and Iwasita, T. (2006). Adsorbed Intermediates of Formaldehyde Oxidation and Their Role in the Reaction Mechanism. *Langmuir* 22, 7912-7916. <https://doi.org/10.1021/la061182z>.

66. Bolzán, A.E., and Arvia, A.J. (1994). Changes in the kinetics of the oxygen evolution reaction induced by oxide films at platinum electrodes. *J. Electroanal. Chem.* 375, 157-162. [https://doi.org/10.1016/0022-0728\(94\)03396-X](https://doi.org/10.1016/0022-0728(94)03396-X).

67. Conway, B.E., Liu, T.C., and Parsons, R. (1997). Examination of electrocatalysis in the anodic O₂ evolution reaction at Pt through evaluation of the adsorption behaviour of kinetically involved intermediate states. *Proc. R. Soc. London, A.* 429, 375-397. <https://doi.org/10.1098/rspa.1990.0065>.

68. Rocha, R.S., Reis, R.M., Lanza, M.R.V., and Bertazzoli, R. (2013). Electrosynthesis of methanol from methane: The role of V₂O₅ in the reaction selectivity for methanol of a TiO₂/RuO₂/V₂O₅ gas diffusion electrode. *Electrochim. Acta* 87, 606-610. <https://doi.org/10.1016/j.electacta.2012.09.113>.

69. Li, J., Yao, L., Wu, D., King, J., Chuang, S.S.C., Liu, B., and Peng, Z. (2022). Electrocatalytic methane oxidation to ethanol on iron-nickel hydroxide nanosheets. *Appl. Catal. B.* 316, 121657. <https://doi.org/10.1016/j.apcatb.2022.121657>.

70. Song, Y., Zhao, Y., Nan, G., Chen, W., Guo, Z., Li, S., Tang, Z., Wei, W., and Sun, Y. (2020). Electrocatalytic oxidation of methane to ethanol via NiO/Ni interface. *Appl. Catal. B.* 270, 118888. <https://doi.org/10.1016/j.apcatb.2020.118888>.

71. Shen, K., Kumari, S., Huang, Y.-C., Jang, J., Sautet, P., and Morales-Guio, C.G. (2023). Electrochemical Oxidation of Methane to Methanol on Electrodeposited Transition Metal Oxides. *J. Am. Chem. Soc.* 145, 6927-6943. <https://doi.org/10.1021/jacs.3c00441>.

72. Ruge, M., Drnec, J., Rahn, B., Reikowski, F., Harrington, D.A., Carlà, F., Felici, R., Stettner, J., and Magnussen, O.M. (2017). Structural Reorganization of Pt(111)

Electrodes by Electrochemical Oxidation and Reduction. *J. Am. Chem. Soc.* **139**, 4532-4539. <https://doi.org/10.1021/jacs.7b01039>.

73. Jerkiewicz, G., Vatankhah, G., Lessard, J., Soriaga, M.P., and Park, Y.-S. (2004). Surface-oxide growth at platinum electrodes in aqueous H₂SO₄: Reexamination of its mechanism through combined cyclic-voltammetry, electrochemical quartz-crystal nanobalance, and Auger electron spectroscopy measurements. *Electrochim. Acta* **49**, 1451-1459. <https://doi.org/10.1016/j.electacta.2003.11.008>.

74. Conway, B.E. (1995). Electrochemical oxide film formation at noble metals as a surface-chemical process. *Prog. Surf. Sci.* **49**, 331-452. [https://doi.org/10.1016/0079-6816\(95\)00040-6](https://doi.org/10.1016/0079-6816(95)00040-6).

75. Lopes, P.P., Strmcnik, D., Tripkovic, D., Connell, J.G., Stamenkovic, V., and Markovic, N.M. (2016). Relationships between Atomic Level Surface Structure and Stability/Activity of Platinum Surface Atoms in Aqueous Environments. *ACS Catal.* **6**, 2536-2544. <https://doi.org/10.1021/acscatal.5b02920>.

76. Angerstein-Kozlowska, H., Conway, B.E., Hamelin, A., and Stoicoviciu, L. (1986). Elementary steps of electrochemical oxidation of single-crystal planes of Au—I. Chemical basis of processes involving geometry of anions and the electrode surfaces. *Electrochim. Acta* **31**, 1051-1061. [https://doi.org/10.1016/0013-4686\(86\)80020-2](https://doi.org/10.1016/0013-4686(86)80020-2).

77. Angerstein-Kozlowska, H., Conway, B.E., Hamelin, A., and Stoicoviciu, L. (1987). Elementary steps of electrochemical oxidation of single-crystal planes of Au Part II. A chemical and structural basis of oxidation of the (111) plane. *J. Electroanal. Chem. Interfacial Electrochem.* **228**, 429-453. [https://doi.org/10.1016/0022-0728\(87\)80122-5](https://doi.org/10.1016/0022-0728(87)80122-5).

78. Peuckert, M., Coenen, F.P., and Bonzel, H.P. (1984). On the surface oxidation of a gold electrode in 1N H₂S₀4 electrolyte. *Surf. Sci.* **141**, 515-532. [https://doi.org/10.1016/0039-6028\(84\)90146-8](https://doi.org/10.1016/0039-6028(84)90146-8).

79. Juodkazis, K., Juodkazytė, J., Jasulaitienė, V., Lukinskas, A., and Šebeka, B. (2000). XPS studies on the gold oxide surface layer formation. *Electrochim. Commun.* **2**, 503-507. [https://doi.org/10.1016/S1388-2481\(00\)00069-2](https://doi.org/10.1016/S1388-2481(00)00069-2).

80. Diaz-Morales, O., Calle-Vallejo, F., de Munck, C., and Koper, M.T.M. (2013). Electrochemical water splitting by gold: evidence for an oxide decomposition mechanism. *Chem. Sci.* **4**, 2334-2343. <https://doi.org/10.1039/C3SC50301A>.

81. Schneeweiss, M.A., and Kolb, D.M. (1997). Oxide formation on Au(111) an in situ STM study. *Solid State Ionics* **94**, 171-179. [https://doi.org/10.1016/S0167-2738\(96\)00587-5](https://doi.org/10.1016/S0167-2738(96)00587-5).

82. van Spronsen, M.A., Frenken, J.W.M., and Groot, I.M.N. (2017). Surface science under reaction conditions: CO oxidation on Pt and Pd model catalysts. *Chem. Soc. Rev.* **46**, 4347-4374. <https://doi.org/10.1039/C7CS00045F>.

83. Grdeń, M., Łukaszewski, M., Jerkiewicz, G., and Czerwiński, A. (2008). Electrochemical behaviour of palladium electrode: Oxidation, electrodissolution and ionic adsorption. *Electrochim. Acta* **53**, 7583-7598. <https://doi.org/10.1016/j.electacta.2008.05.046>.

84. Birss, V.I., Chan, M., Phan, T., Vanýsek, P., and Zhang, A. (1996). An electrochemical study of the composition of thin, compact Pd oxide films. *J. Chem. Soc., Faraday Trans.* **92**, 4041-4047. <https://doi.org/10.1039/FT9969204041>.

85. Bolzán, A.E., Martins, M.E., and Arvíá, A.J. (1983). The complex processes involved at Pd electrodes in 1 M H₂SO₄ in the potential range of oxygen electroadsorption-electrodesorption reactions. *J. Electroanal. Chem. Interfacial Electrochem.* 157, 339-358. [https://doi.org/10.1016/S0022-0728\(83\)80361-1](https://doi.org/10.1016/S0022-0728(83)80361-1).

86. Haan, J.L., and Masel, R.I. (2009). The influence of solution pH on rates of an electrocatalytic reaction: Formic acid electrooxidation on platinum and palladium. *Electrochim. Acta* 54, 4073-4078. <https://doi.org/10.1016/j.electacta.2009.02.045>.

87. Fornaciari, J.C., Primc, D., Kawashima, K., Wygant, B.R., Verma, S., Spanu, L., Mullins, C.B., Bell, A.T., and Weber, A.Z. (2020). A Perspective on the Electrochemical Oxidation of Methane to Methanol in Membrane Electrode Assemblies. *ACS Energy Lett.* 5, 2954-2963. <https://doi.org/10.1021/acsenergylett.0c01508>.

88. Ge, L., Rabiee, H., Li, M., Subramanian, S., Zheng, Y., Lee, J.H., Burdyny, T., and Wang, H. (2022). Electrochemical CO₂ reduction in membrane-electrode assemblies. *Chem* 8, 663-692. <https://doi.org/10.1016/j.chempr.2021.12.002>.

89. Huang, G., Mandal, M., Hassan, N.U., Groenhout, K., Dobbs, A., Mustain, W.E., and Kohl, P.A. (2021). Ionomer Optimization for Water Uptake and Swelling in Anion Exchange Membrane Electrolyzer: Hydrogen Evolution Electrode. *J. Electrochem. Soc.* 168, 024503. <https://doi.org/10.1149/1945-7111/abde7b>.

90. Huang, G., Mandal, M., Hassan, N.U., Groenhout, K., Dobbs, A., Mustain, W.E., and Kohl, P.A. (2020). Ionomer Optimization for Water Uptake and Swelling in Anion Exchange Membrane Electrolyzer: Oxygen Evolution Electrode. *J. Electrochem. Soc.* 167, 164514. <https://doi.org/10.1149/1945-7111/abcde3>.

FIGURE TITLES AND LEGENDS

Figure 1. Effect of ion transport on product distribution during AcOR

(A), (C), (E-F) Time dependent (A), (C), (E) measured concentration and F) relative concentration of the products obtained during the oxidation of (A), (E), (F) 0.5 M and (C) 5.0 M CH₃COOK over Pt electrode at 3.2 V using (A), (C) Nafion®-117 membrane and (E), (F) A-201 membrane (See also Figures S1-S4). Insets: the zoomed version of the respective concentration plots at specific time lengths.
(B), (D) Schematic of the AcOR process in a batch cell with (B) PEM and (D) AEM.

Figure 2. Impact of pulse electrolysis on product evolution

Relative concentration of the products obtained during the AcOR in a 1.5 M CH₃COOK electrolyte over Pt electrodes having A-201 membrane with an applied potential of 3.2 V and a pulse at 0.5 V at 2 h interval for 60s (See also Figure S7).

Figure 3. Mechanistic pathways of AcOR products via isotope labelling

Proposed mechanism of product formation during acetate oxidation with the aid of the compounds identified through the isotope labeling experiments conducted using CH₃¹³COONa (cyan) and ¹³CH₃COONa (red). (Condensation in the path [13] refers to the removal of a water molecule. For reaction pathways of further oxidation of methanol and formaldehyde mentioned in the path [12], please refer^{59,60}. See also Figures S8-S11)

Figure 4. AcOR over various noble metal anodes

(A), (C), (E) Product distribution obtained during electrochemical oxidation of acetate over (A) Pt, (C) Au and (E) Pd anode in 0.5 M CH₃COOK.
(B), (D), (F) Cyclic voltammograms of (B) Pt, (D) Au and (F) Pd anode taken at a scan rate of 100 mV s⁻¹ before and after electrolysis in 0.5 M CH₃COOK (See also Figure S12).

Figure 5. Changes in product formation on noble metal anodes with an AEM separator and 1.5M CH₃COOK electrolyte

(A-C) Product distribution obtained during the electrochemical oxidation of 1.5 M CH₃COOK over (A) Pt, (B) Au, and (C) Pd metal electrodes using A-201 membrane (See also Figures S13-S15).

Figure 6. AcOR in a MEA-based flow cell

(A) Schematic of AcOR in an MEA-based flow cell.
(B) Comparison of product distribution achieved with Pt catalyst in an MEA-based flow cell and noble metals in a batch cell.